Monitoring of the Spatio-Temporal Dynamics of the Floods in the Guayas Watershed (Ecuadorian Pacific Coast) Using Global Monitoring ENVISAT ASAR Images and Rainfall Data

Frédéric Frappart, Luc Bourrel, Nicolas Brodu, Ximena Riofrío Salazar, Frédéric Baup, José Darrozes, Rodrigo Pombosa

water

MDPI

Article

Monitoring of the Spatio-Temporal Dynamics of the Floods in the Guayas Watershed (Ecuadorian Pacific Coast) Using Global Monitoring ENVISAT ASAR Images and Rainfall Data

Frédéric Frappart [1,2,*], Luc Bourrel [1,*], Nicolas Brodu [3], Ximena Riofrío Salazar [1,4], Frédéric Baup [5], José Darrozes [1] and Rodrigo Pombosa [6]

1 Géosciences Environnement Toulouse (GET), UMR 5563, CNRS/IRD/UPS, Observatoire Midi-Pyrénées (OMP), 14 Avenue Edouard Belin, 31400 Toulouse, France; ximena.riofrio@gmail.com (X.R.S.); jose.darrozes@get.omp.eu (J.D.)

2 Laboratoire d'Etudes en Géophysique et Océanographie Spatiales (LEGOS), UMR 5566, CNRS/IRD/UPS, Observatoire Midi-Pyrénées (OMP), 14 Avenue Edouard Belin, 31400 Toulouse, France

3 Inria Bordeaux Sud-Ouest, Géostat, 200 Avenue de la Vieille Tour, 33405 Talence, France; nicolas.brodu@inria.fr

4 Secretaría de Educación Superior, Ciencia y Tecnología (SENESCYT), Whymper E7-37 y Alpallana, 170516 Quito, Ecuador

5 Centre d'Etudes Spatiales de la BIOsphère (CESBIO), UMR5126, UPS/CNRS/IRD/CNES, Observatoire Midi-Pyrénées (OMP), 14 Avenue Edouard Belin, 31400 Toulouse, France; frederic.baup@cesbio.cnes.fr

6 Instituto Nacional de Meteorología e Hidrología (INAMHI), Iñaquito N36-14 y Corea, 160310 Quito, Ecuador; rpombosa@inamhi.gob.ec

* Correspondence: frederic.frappart@legos.obs-mip.fr (F.F.); luc.bourrel@ird.fr (L.B.)

Academic Editor: Hongjie Xie
Received: 13 November 2016; Accepted: 21 December 2016; Published: 1 January 2017

Abstract: The floods are an annual phenomenon on the Pacific Coast of Ecuador and can become devastating during El Niño years, especially in the Guayas watershed (32,300 km^2), the largest drainage basin of the South American western side of the Andes. As limited information on flood extent in this basin is available, this study presents a monitoring of the spatio-temporal dynamics of floods in the Guayas Basin, between 2005 and 2008, using a change detection method applied to ENVISAT ASAR Global Monitoring SAR images acquired at a spatial resolution of 1 km. The method is composed of three steps. First, a supervised classification was performed to identify pixels of open water present in the Guayas Basin. Then, the separability of their radar signature from signatures of other classes was determined during the four dry seasons from 2005 to 2008. In the end, standardized anomalies of backscattering coefficient were computed during the four wet seasons of the study period to detect changes between dry and wet seasons. Different thresholds were tested to identify the flooded areas in the watershed using external information from the Dartmouth Flood Observatory. A value of -2.30 ± 0.05 was found suitable to estimate the number of inundated pixels and limit the number of false detection (below 10%). Using this threshold, monthly maps of inundation were estimated during the wet season (December to May) from 2004 to 2008. The most frequently inundated areas were found to be located along the Babahoyo River, a tributary in the east of the basin. Large interannual variability in the flood extent is observed at the flood peak (from 50 to 580 km^2), consistent with the rainfall in the Guayas watershed during the study period.

Keywords: flood; SAR; ENVISAT ASAR; rainfall; Guayas; Ecuadorian Pacific slope

1. Introduction

El Niño Southern Oscillation (ENSO) has a strong influence on rainfall patterns on the Pacific Coast of South America, from Ecuador to Chile, at an interannual time scale e.g., [1–4], affecting the likelihood of droughts and floods [5]. Positive anomalies of sea surface temperatures along the coast of Peru and Ecuador occurring during ENSO events induced torrential rains that cause high discharge and large flood events [6]. In the Guayas Basin, located in the southwest of Ecuador, in the Pacific slope of the Andes Cordillera, large flood events that occurred during the major El Niño episodes of 1965–1966, 1972–1973, 1982–1983, and especially 1997–1998, were responsible for many casualties and had important socio-economic impacts on housing, agriculture, and fisheries [7].

Data acquired by in situ hydrometeorological networks and remotely sensed images are commonly used for monitoring the spatial extent of the floods and even for forecasting and warning [8,9]. In spite of the good spatial and temporal resolutions of multispectral images, their use is limited in tropical areas as they are vulnerable to cloud cover and unable to detect water under dense vegetation cover. In the Guayas Basin, the almost permanent cloud cover during the rainy season does not allow the use of multispectral images, even the high frequency daily or the 8-day composite MODIS reflectance products, to monitor the temporal variations of the flood extent. Synthetic Aperture Radar (SAR) images, that provide useful information under all-weather conditions, including cloud cover, have been widely used for flood mapping and wetland delineation, especially at L-band as this microwave frequency band is able to penetrate dense vegetation cover e.g., [10–13]. Nevertheless, L-band images acquired by sensors such as JERS-1, PALSAR onboard ALOS (repeat-period of 46 days), did not have a sufficient temporal resolution to be used for flood monitoring. Images from PALSAR-2 on-board ALOS-2, available since May 2014, were not considered as they only cover two rainy seasons in the Guayas watershed. Several studies showed that SAR images acquired at the higher C-band frequency can also be used for detecting floods in less vegetated areas e.g., [14–17]. SAR images acquired in Wide Swath (WS) mode by the Advanced SAR (ASAR) onboard ENVISAT, at a spatial resolution of 150 m, were widely used for the monitoring of flood dynamics from local to regional scales [16–19]. Only 29 ASAR images were acquired in WS mode between November 2002 and March 2012 and just 14 during the rainy seasons due to acquisitions in other modes. No images were acquired during the 2004, 2005 and 2009 rainy seasons, and only two or three the other years, for a rainy season that last 6 months. The low number of available ASAR WS images is insufficient to allow the monitoring of the time variations of the flood in the Guayas watershed. Images acquired by ASAR in Scan SAR Global Monitoring (GM) mode at coarse spatial resolution (1 km), for a temporal resolution generally better than one month, offered the opportunity to monitor inundation extents from regional to global scales [20–22]. Before the launch of Sentinel-1 that has been providing high resolution images (20 m of spatial resolution) with a temporal sampling of a few days since April 2014, ASAR images acquired in GM mode had the advantages to provide frequent (twice or third a month) observations of the same scene and to provide a complete observation of medium-size watershed in one acquisition.

In this study, we used ENVISAT ASAR images acquired in GM mode to monitor the floods in the Guayas watershed between 2005 and 2008. We first present the study area and the datasets. Then, we describe the change detection method used for determining the inundation extent in each image. The last part presents a sensitivity analysis of the change detection method, the spatio-temporal variations of the flood extent and the relationship between the time-series of rainfall and inundation extent during the observation period.

2. Study Area

The Guayas River Basin, located in the southwestern part of Ecuador, is the largest tropical agricultural watershed and estuarine system of the Pacific slope of South America. It extends between latitudes 0° S and 3° S, and longitudes 81° W and 78° W and covers an area of 32,300 km^2 (Figure 1). Its watershed represents 13% of the total area of Ecuador where 40% of the Ecuadorian population lives [23]. It corresponds to the most productive region of Ecuador for agriculture and aquaculture [24].

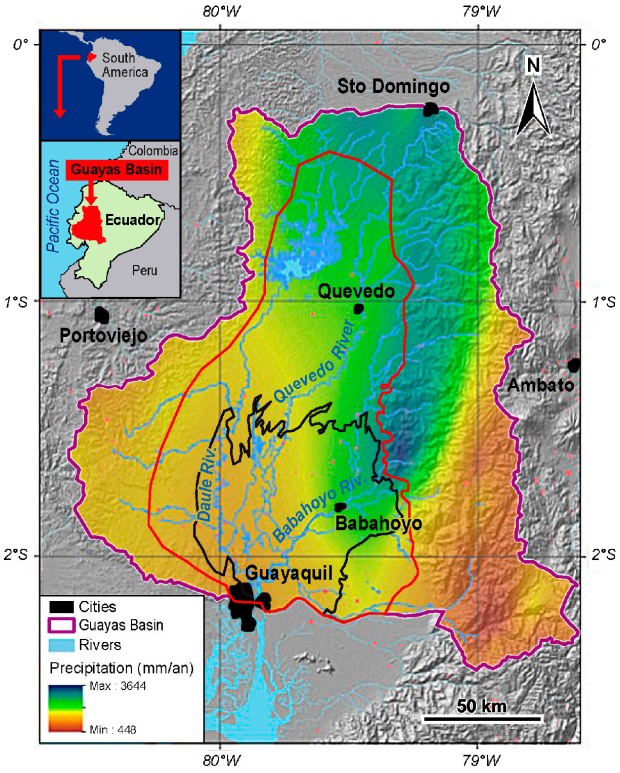

Figure 1. The Guayas Basin (boundary in purple) is located in the southwest Pacific slope of Ecuadorian Andes. The lowland (boundary in red) occupies 15,000 km^2 of the 32,300 km^2 of the watershed area, and the floodplain 5000 km^2. The mean annual rainfall isohyets map was elaborated for the 1963–2009 period using cokriging method.

Its climate is characterized by the occurrence of the rainy season from December to May. The average precipitation in the Guayas basin for the 1963–2009 period is 1849 mm during the hydrological year and 1130 mm during the rainy season. This value increased respectively to 4769 mm, 2412 mm and 6786 mm for the El Niño episodes of 82–83, 91–92 and 97–98, corresponding respectively to ratios El Niño/Normal events of 2.6, 1.3 and 3.7 [25].

The altitude of this drainage basin ranges from sea level to 6310 m at Mount Chimborazo in the Andes Cordillera. The lower plain of the Guayas Basin is the region corresponding to altitudes lower than 200 m. Its area is ~15,000 km^2 [23], i.e., ~46% of the surface of the watershed. In this lower plain, the region likely to be affected by floods corresponds to almost flat areas (slopes $\leq$ 5%). They represent 30% of the lower plain or ~5000 km^2.

The Daule, Babahoyo and Quevedo Rivers are the largest tributaries of western and eastern parts that merge downstream to form the Guayas River and subsequently the Guayas Estuary that flow into the Gulf of Guayaquil (Figure 1). The mean discharge to the sea of the Guayas River varies from 200 m^3/s during the dry season to 1600 m^3/s at the peak of flow [26,27]. It can reach up to 5000 m^3/s during strong ENSO events as 1982/1983 or 1997/1998 [26].

3. Datasets

3.1. ENVISAT ASAR GM Mode Images

ENVISAT mission was launched on 1 March 2002 by the European Space Agency (ESA). It orbits at an average altitude of 790 km, with an inclination of 98.54°, on a sun-synchronous orbit with a 35-day repeat cycle. It carried 10 scientific instruments including ASAR operating at a central frequency of 5.331 GHz (C-band). This sensor offered multiple acquisition modes for SAR images at various

spatial and temporal resolutions and alternating polarizations. Among them, the ScanSAR GM mode acquired images in a swath of 405 km at a spatial resolution of 1 km and temporal resolution between four and seven days when no other acquisition in a different mode was ordered [28]. This mode is very useful for the monitoring of dynamic processes, such as soil moisture or floods, from regional to global scales e.g., [20–22,29,30]. In this study, we used 92 ASAR images acquired in GM mode, with HH polarization and 1 km spatial resolution, from December 2004 to September 2008, that encompass the whole Guayas Basin (Figure 2). HH polarization is the more adequate polarization for flood mapping on ASAR [31]. During the rainy season, there is generally one acquisition every two weeks at least that covers the whole basin.

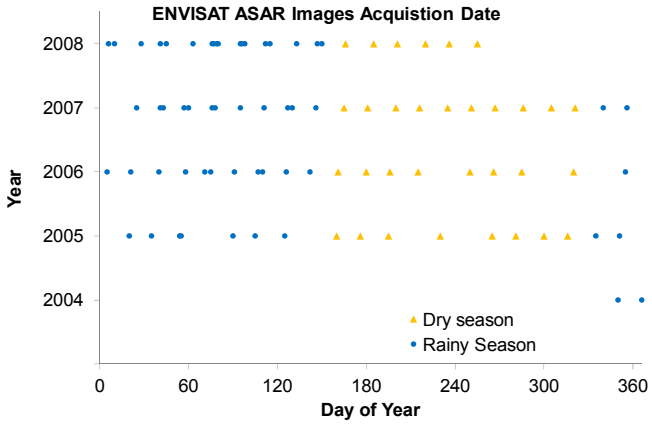

Figure 2. Acquisition dates of ENVISAT ASAR images in GM mode over the Guayas Basin between December 2004 and September 2008 for dry (orange squares) and rainy (blue dots) seasons. These images were made available by ESA through the EOLi (Earth Observation Link) Earth Observation Catalogue and Ordering Services [32].

3.2. Land Cover Map of Ecuador

A land cover map of the Ecuador was produced by the Ecuadorian Ministry of Agriculture (Ministerio de Agricultura, Ganadería, Acuacultura y Pesca—MAGAP) in 2002 over the whole country at the spatial scale of 1:250,000 using Landsat TM multispectral images acquired between 1999 and 2001 validated with a ground control assessment performed in 2001–2002. The main land cover types present in the Guayas watershed are the following:

(i) forests (native and cultivated) occupying an area of 9206 km^2 (29% of the watershed area), permanent crops including banana, sugar cane, fruit trees, plantain, African palm, cacao, and coffee occupying an area of 6087 km^2 (20% of the watershed area),
(ii) annual crops including corn, rice, soybeans, and vegetables occupying an area of 9181 km^2 (29% of the watershed area),
(iii) pastures occupying an area of 4130 km^2 (13% of the watershed area), water bodies occupying an area of 487 km^2 (2% of the watershed area), urban areas occupying an area of 223 km^2 (1% of the watershed area).

More details about intra-class land cover repartition can be found in [33].

3.3. Surface Water Record from the Dartmouth Flood Observatory

The Dartmouth Flood Observatory (DFO) provides a unique source of information on floods due to its global coverage [34]. It comprises the Surface Water Record (SWR), a comprehensive record of satellite-observed changes in the Earth's inland surface waters. This dataset compiles the observed history of flooding, starting in the year 2000. Extent of surface water is mostly derived from NASA's MODIS Terra and Aqua sensors with, in some cases, additional information from Radarsat, ASTER,

or other higher spatial resolution data [35]. Water areas are accumulated over 10 days to minimize the effect of cloud cover. Inundation maps are made available at a spatial resolution of 250 m on 10° × 10° tiles. A color code indicates maximum flood extent each year. It is important to note, that using this representation mode, it is impossible to know how many times a pixel was inundated during the observation period. Besides, this dataset does not allow the monitoring of the variations of flood extent during the hydrological cycle. A specific color indicates the reference water status (February, 2000, from the Shuttle Radar Topography Mission Water Body—SWBD data). In the case of the Guayas Basin, MODIS images during the rainy season cannot be used due to the cloud cover. So, this dataset is limited to SWBD in this specific area completed with the inundation extent observed during the two large flood events of 1998 and 2002. In our study, it is used as static information on the maximum flood extent in the Guayas Basin. The flood extent image encompassing the eastern part of the basin (east of 80° W of longitude) was downloaded at the Flood Observatory [36]. No data are available for the western part that corresponds to the western tributaries of the Daule River and a part of its stream.

3.4. Rainfall

Monthly rainfall records from 310 meteorological stations located over the Pacific slope of the Ecuadorian Andes (5° S–1.5° N and 77.5° W–81° W) were provided by INAMHI (National Institute of Meteorology and Hydrology of Ecuador) from 1963 to 2009. A careful quality check of this data was performed using the regional vector method similarly to what was performed in [3,4]. This dataset was interpolated at a spatial resolution of 1 km using a co-kriging method as in [4].

4. Methods

The methodology used to process the time series of SAR images is composed of the following three main steps: the preprocessing of the SAR images, the classification of the SAR images acquired during the dry season for land cover purposes and assessment of the characterization of the radar backscattering response between open water and non-inundated surfaces during the dry season, and the flood detection during the dry season (Figure 3).

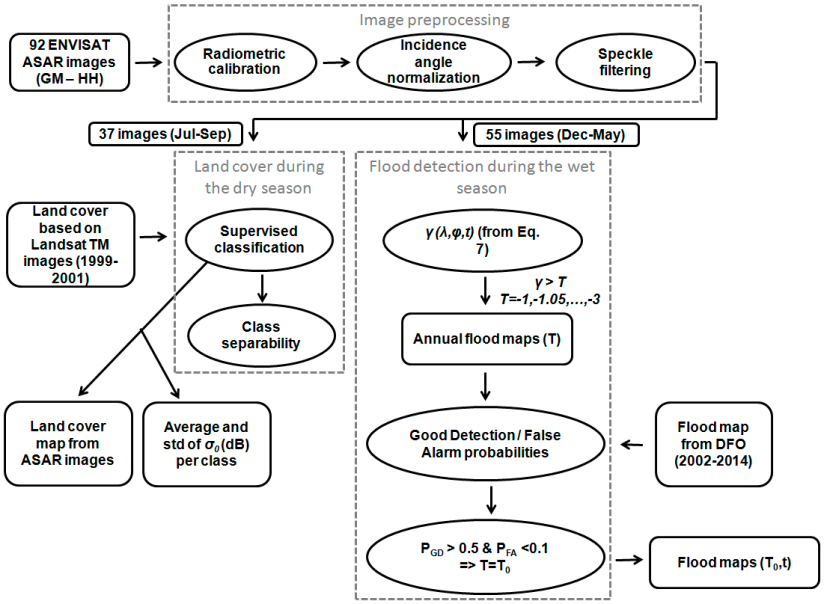

Figure 3. Schematic view of the processing of the ENVISAT ASAR images acquired in GM mode between December 2004 and September 2008. The method is composed of three steps: a pre-processing of the images, a supervised classification to determine the land cover using the images acquired during the dry season (July–September), the change detection method applied to monitor the flood extent during the wet season (December–May).

4.1. ENVISAT ASAR GM Mode Images Preprocessing

The ASAR GM images were preprocessed with respect to the following steps: radiometric calibration, incidence angle normalization, speckle reduction and geometrically correction using the Next ESA SAR Toolbox (NEST) [37]. Images of radar backscattering coefficients (σ_0 or sigma naught) at the incidence angle θ of acquisition of each image were derived from the brightness amplitudes expressed in Digital Numbers (DN) in the ASAR GM products using:

$$\sigma_0(\theta) = \frac{DN^2}{K} \sin\theta \quad (1)$$

where K is the absolute calibration constant [38].

The effect of the incidence angle on the surface backscattering was taken into account through a normalization procedure [39]. The normalized backscatter coefficient is given by:

$$\sigma_0{}^{norm} = \frac{\sigma_0(\theta)}{F(\theta)} \quad (2)$$

where $F(\theta)$ is a peculiar function to the target environmental conditions that has the following form [39,40]:

$$F(\theta) = \cos^{\alpha}\theta \quad (3)$$

where α is a coefficient depending on the predominant scattering mechanism and the sensor condition [41].

In the following, $\sigma_0{}^{norm}$ is noted σ_0 for simplification.

Finally, the radar images were spatially filtered to reduce speckle effects using a classical Lee filter [42] with a window size of 5 by 5 pixels. Examples of resulting images are presented in Figure 4a,b for dry and rainy seasons, respectively.

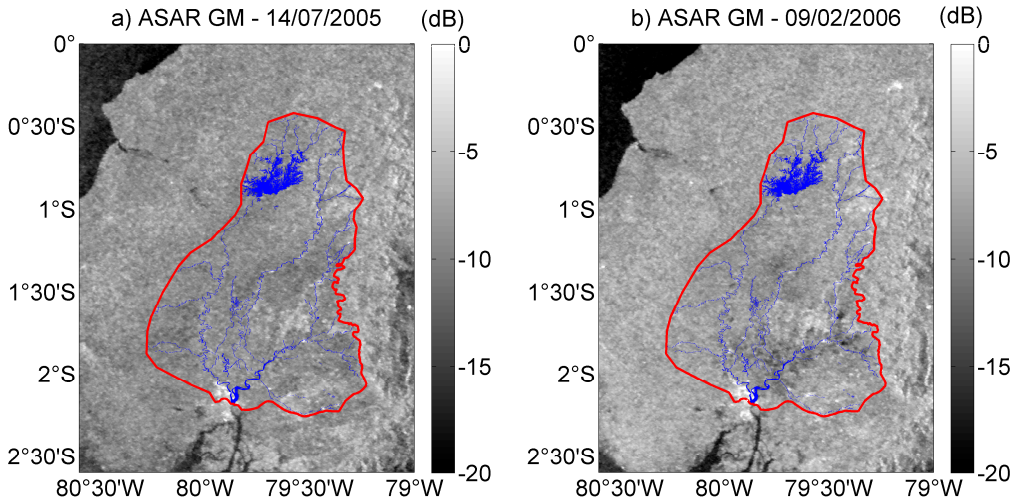

Figure 4. Images of backscattering obtained after the pre-processing of ENVISAT ASAR images in GM mode acquired during the (**a**) dry (14 July 2005); and (**b**) rainy (9 February 2006) seasons in the Guayas Basin lowland. The boundary of the lowland is represented using a red line and open water appears in blue.

4.2. Land Cover during the Dry Season Using a Supervised Classification

The change detection method used to identify flooded pixels during the wet season requires a well-defined initial state corresponding to the backscattering during the dry season. It is necessary to check the separability of the class corresponding to water from the other classes. Eleven supervised

classifications were performed on 37 ASAR images acquired during the dry seasons, from July to September, over 2005–2008 and not only the maximum of likelihood technique as done previously in [43].

The feature space consists of all dry season backscattering coefficients for each given pixel. Classifiers thus work in a large dimensional vector space and discriminate seasonal patterns of each of the five classes present in the Guayas watershed according to the Landsat TM-based land use map: water bodies (lakes, rivers), permanent crops (palm trees, cocoa, bananas, coffee), seasonal crops (rice, corn, soy), grazing fields, cities. The training data were chosen using the land use map defined in 2002 using Landsat TM images. The selected training sites (2292 pixels randomly selected in the land use map) correspond to the five classes present in the Guayas watershed according to the Landsat TM-based land use map. A 10-fold cross-validation was used to set the meta-parameters (e.g., K in k-nearest neighbors) and report the corresponding accuracy as the performance metric for each classifier in Section 5 (Results). As the results of the classification during the dry season are used in the followings for detecting changes in backscattering related to floods, it is necessary to choose the method that provides the best results in terms of accuracy. The separability between the classes was assessed using:

(i) the M-statistics, originally introduced to discriminate burned and unburned pixels in multi-spectral images [44], was also applied to SAR images in land use applications [45]. It is computed as follows:

$$M = \frac{\mu_i - \mu_j}{\sigma_i - \sigma_j} \tag{4}$$

where σ_k and μ_k are the mean and standard deviation of the kth class respectively. M values greater than 1 indicate a reasonable separability increasing with the value of M.

(ii) the Jeffries-Matusita distance defined as follows [46]:

$$d_{J-M}(i,j) = \sqrt{2(1 - e^{-\alpha})} \tag{5}$$

with

$$\alpha = \frac{1}{2}(\mu_i - \mu_j)^T \left(\frac{C_i + C_j}{2}\right)^{-1} (\mu_i - \mu_j) + \frac{1}{2} \ln \left(\frac{\frac{1}{2}|C_i + C_j|}{\sqrt{|C_i||C_j|}} \right) \tag{6}$$

where C_k is the covariance matrix of the kth class. It varies from 0 (no separation) to $\sqrt{2}$–1.41 (complete separation).

4.3. Flood Detection

A change detection method was applied to the ASAR images acquired during the rainy seasons between 2005 and 2008. For each pixel of coordinates (λ, φ) of any 55 ASAR images acquired during the wet season at time t, we computed the following normalized anomaly of σ_0 (γ), defined as follows:

$$\gamma(\lambda, \varphi, t) = \frac{\sigma_0(\lambda, \varphi, t) - \langle \sigma_0(\lambda, \varphi, t) \rangle_{dry}}{std(\sigma_0(\lambda, \varphi, t))_{dry}} \tag{7}$$

where $<\sigma_0(\lambda,\varphi,t)>_{dry}$ and $std(\sigma_0(\lambda,\varphi,t))_{dry}$ are the average and the standard deviation of σ_0 during the 2005–2008 dry seasons, respectively.

Flooded pixels present lower backscattering than bare soil or vegetation covered ones as the radar electromagnetic wave is specularly reflected by water surfaces. As a consequence, the lower γ is, the more inundated the pixel is. As the vegetation cover in the lowland of the Guayas Basin is not composed of forests, but of pastures, seasonal and permanent crops, the presence of water under vegetation will cause a decrease in radar backscattering e.g., [14]. The risk to have $std(\sigma_0(\lambda,\varphi,t))_{dry}$ close

to zero is limited at the spatial resolution of 1 km. The only available external source of information on the flood in the Guayas watershed is the SWR from the DFO. Most of the flooded areas present in the SWR since 2000 have their extent included in the previous large flood events of 2002, and especially 1998. This dataset is commonly used for estimating flood extent limits when processing other remotely sensed observations e.g., [47,48]. Our goal is to determine a threshold to discriminate changes caused by the floods from changes in land cover, due to the vegetation growth, or due to the presence of soil moisture. We determined the number of inundated and falsely inundated pixels in this watershed using the surface water extent 2000–2014 from the DFO SWR for each value of γ varying from -1 to -3 with a step of 0.05 as follows:

(i) for each ASAR image, a binary image representing the flood extent at time t is obtained: all ASAR pixels with values lower or equal to γ are considered flooded and pixels with values greater than γ not flooded.
(ii) annual maps of maximum flood extent are then obtained. In these maps, a pixel is considered to be well identified as flooded if it is also inundated in the SWR whereas it is badly identified as if it is not also identified as inundated in the SWR.
(iii) annual ratios of good and false detections are determined as the numbers of well and falsely detected as inundated pixels divided by the numbers of pixels identified as inundated and non-inundated in the DFO SWR, respectively.

Thresholds on good and false detections allow the determination of the value of the threshold on γ. For every value of γ, the inundated area S is then estimated as follows:

$$S(t) = R_e^2 \sum_{i \in A} \delta(\lambda_i, \varphi_i, t) \cos(\varphi_i) \Delta\lambda \Delta\varphi \quad (8)$$

where R_e the radius of the Earth equals 6378 km, λ_i and φ_i are the longitude and latitude of the ith pixel inside the Guayas watershed of area A, $\delta(\lambda_i,\varphi_i,t)$ equals one if the pixel is inundated and 0 if not, $\Delta\lambda$ and $\Delta\varphi$ are the grid steps in longitude and latitude, respectively, that are equal to 0.0045°.

4.4. Relative Frequency of Inundation

A relative frequency of inundation (RFI) map, based on the time-series of inundation map derived from the ASAR images acquired between December 2004 and June 2008, was estimated for the Guayas Basin floodplain. Following a method similar to the one proposed by [49], the RFI, expressed in %, of a pixel of geographical coordinates (λ;φ) is defined as follows:

$$RFI(\lambda;\varphi) = \frac{\sum_{n=1}^{N} \delta(\lambda, \varphi, n)}{N} \times 100 \quad (9)$$

where N is the number of images acquired during the rainy season over the whole study period and $\delta(\lambda,\varphi,n)$ equals one if the pixel is inundated and 0 if not.

5. Results

5.1. Land Cover from ASAR GM Images during the Dry Season

The performances of the 11 different techniques (i.e., k-nearest neighbors, linear and Gaussian SVM, random forest, extremely random trees, adaboost, naive Bayes, logit, linear and quadratic discriminants, ridge regression) were assessed in terms of multi-class accuracy (5 classes). Among them, the k-nearest neighbor classification appears to be the most efficient and the most robust for discriminating the classes based on their temporal patterns in the dry season with an accuracy of 98.2% $\pm$ 0.7%. In the followings, all the results are presented for this supervised classification. The resulting land cover map derived from the k-nearest neighbor method is presented in Figure 5.

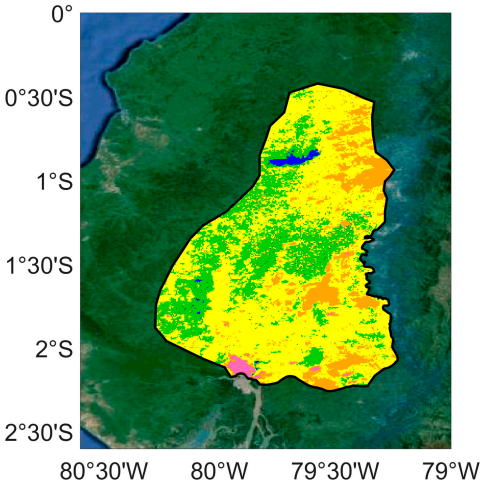

Figure 5. Land use from ENVISAT ASAR GM images acquired during the dry seasons (June to November) between 2005 and 2008, as determined by k-nearest neighbors supervised classification. The resulting classes are the followings: open water (blue), permanent crops (green), seasonal crops (orange), grazing fields (yellow), cities (pink). The boundary of the lowland is represented using a black line. Background image is from Google Maps.

The five classes correspond to open water (lakes and reservoirs) as the Guayas river stream and its tributaries cannot be identified at a spatial resolution of 1 km, permanent crops composed of tropical arboriculture (banana, oil palm, coffee and cacao trees), seasonal crops (mostly rice, corn, soya, and shrubby vegetation), mostly pastures and sugar cane, towns, respectively.

The results of the class separability are presented in Table 1. It appears clearly that the different classes are well separated from one another using both criteria, especially using the Jeffries-Matusita distance. The Jeffries-Matusita distance between each pair of classes is higher than 1.40 except between permanent crops and seasonal crops. In this case, its value is 1.34 which corresponds to a good separation between the two classes as this value is quite close to the maximum value of the Jeffries-Matusita distance ($\sqrt{2}$). Very good separability is also observed using the M-statistics ($M > 1$), except for the separability with cities class, due to the large standard deviation (see Table 2) observed in this class, a consequence of the low spatial resolution of the ENVISAT ASAR GM images (1 km). However, even for this class, the M-statistics present values close to 1 or a little bit higher (Table 1). In all cases, a good separability is observed between open water and the other classes.

Table 1. Results of the separability between classes obtained from a k-nearest neighbors supervised classification performed on ENVISAT ASAR GM images acquired during the dry season (July–September) between 2005 and 2008 using the M-statistics and the Jeffries-Matusita distance.

Separability between Classes		Open Water	Permanent Crops	Seasonal Crops	Grazing Fields	Cities
Open water	M-statistics	-	6.67	2.14	4.37	1.08
	J-M	-	1.41	1.41	1.41	1.41
Permanent crops	M-statistics	-	-	1.55	2.91	0.98
	J-M	-	-	1.34	1.41	1.41
Seasonal crops	M-statistics	-	-	-	1.20	0.90
	J-M	-	-	-	1.41	1.41
Grazing fields	M-statistics	-	-	-	-	0.93
	J-M	-	-	-	-	1.41
Cities	M-statistics	-	-	-	-	-
	J-M	-	-	-	-	-

Table 2. Results of the k-nearest neighbors supervised classification performed on ENVISAT ASAR GM images acquired during the dry season (July–September) between 2005 and 2008. For each class, average backscattering (dB), associated standard deviation (dB), and percentage of the watershed area (%) are given.

Dry Season Classification Class Name	Average Backscattering (dB)	Standard Deviation of Backscattering (dB)	Percentage of the Watershed Area (%)
Open water	−11.30	1.68	0.9
Permanent crops	−8.63	1.29	15.0
Seasonal crops	−6.19	1.70	54.0
Grazing fields	−7.65	1.29	29.0
Cities	−1.87	2.74	1.1

Using the results from the k-nearest neighbors supervised classification, land cover in the Guayas watershed is dominated by seasonal crops (54%), characterized by $\sigma_0 = -6.19 \pm 1.70$ dB, followed by grazing fields (29%), with $\sigma_0 = -7.65 \pm 1.29$ dB, permanent crops (15%), with $\sigma_0 = -8.63 \pm 1.29$ dB, cities (1.1%), with $\sigma_0 = -1.87 \pm 2.74$ dB and open water (0.9%), with $\sigma_0 = -11.30 \pm 1.68$ dB (Table 2 and Figure 6).

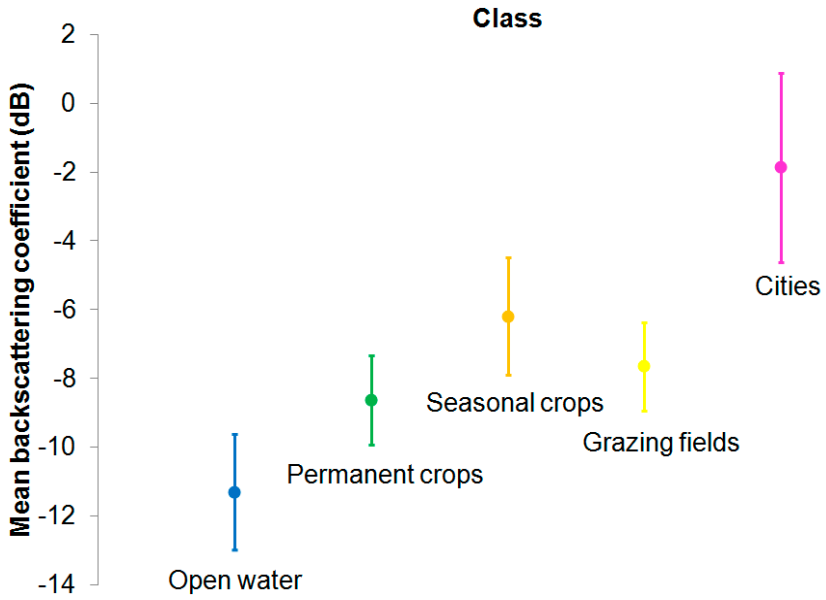

Figure 6. Average backscattering coefficient (dB) and associated standard deviation (dB) for each class resulting from a k-nearest neighbors supervised classification performed during the dry season (July–September) between 2005 and 2008: open water (blue), permanent crops (green), seasonal crops (orange), grazing fields (yellow), cities (pink).

5.2. Flood Detection during the Rainy Season

Normalized anomalies of backscattering γ were computed for the 55 ASAR images acquired during the rainy season using (7). We determined the number of pixels whose value is beyond the threshold for each rainy season from 2005 to 2008 for threshold values varying from −1 to −3 with a step of −0.05. These pixels are then considered as flooded and can be used to estimate annual maps of inundation when stacking the binary images of floods during each year's rainy season. The range of the threshold values corresponds to intervals of confidence varying from 68.3% to 99.7% compared to its value during the dry season, according to the three-sigma rule of thumb assuming a normal distribution of the data.

Examples of resulting maps for different threshold values are presented in Figure 7 for 2008 that was the wetter year of the observation period. Compared to the SWR from DFO (Figure 7a), lower threshold values led to flooded areas in excess (for instance, thresholds of −1.0 and −1.5 in Figure 7b,c), whereas flood maps obtained using higher threshold values present very limited inundated areas (for instance, thresholds of −2.5 and −3.0 in Figure 7e,f). The map obtained using γ equals to −2.0 exhibits a similar pattern as the SWR (Figure 7a,d, respectively). To more accurately determine the thresholds value, we compared the SWR and γ maps pixel by pixel. A pixel is considered to be well identified as flooded if its value is below the threshold and is inundated in the SWR whereas it is poorly identified as flooded if its value is lower or equal to the threshold but it is not identified as inundated in the SWR. The results of the change detection method limited to the floodplain area are presented on Figure 8. We fixed the following thresholds: as no large ENSO was recorded between 2005 and 2008, we considered that the minimum threshold value for inundated pixels should correspond to a number of pixels higher than 50% of the number of inundated pixels of the SWR in the Guayas floodplain during the wettest year of the study period. According to Figure 8a, it corresponds to a minimum value of γ higher than −2.35. The corresponding ratios are 10.8%, 30.9%, 12.1% and 50.2% for 2005, 2006, 2007, and 2008, respectively. Similarly, the number of pixels falsely detected as inundated should be lower than 10% of the number of inundated pixels of the SWR in the Guayas watershed during the wetter year, considering the possible missed detection of flooded areas in this dataset. According to Figure 8b, it corresponds to a maximum value of γ lower than −2.25. The corresponding ratios are 3.7%, 7.1%, 2.2% and 9.5% for 2005, 2006, 2007, and 2008, respectively. Using these criteria, γ varies between −2.25 and −2.35. Converted (7) into dB, it means that the difference between (i) the change in backscattering between the dry season and the time t during the rainy season; and (ii) the standard deviation of the backscattering during the dry season is greater than 3.52, 3.63 and 3.71 dB for threshold values of −2.25, −2.30, and −2.35, respectively. According to Table 2, these values are larger than the standard deviation of any of the five classes considered in this study. As these classes were found be well separated, it is reasonable to consider that these thresholds can be used for separating inundated and non-inundated pixels. Maximum annual flood extent obtained using thresholds of −2.25, −2.30, −2.35 between 2005 and 2008 are presented in Figure 9. Very similar patterns are observed with the flood extent decreasing with γ. The pattern of inundated areas is very consistent with the hydrological characteristics of the Guayas floodplain. Areas detected as flooded are present along the major tributaries to the Guayas (i.e., Babahoyo, Quevedo, Daule) or in the wetlands such as the RAMSAR site Abras de Mantequilla wetland, located between the Quevedo and Daule rivers, which plays a role in flood attenuation and streamflow regulation [50]. Large interannual variability can also be observed during the 2005–2008 time-span. A more detailed analysis of the results is provided in Section 5.3.

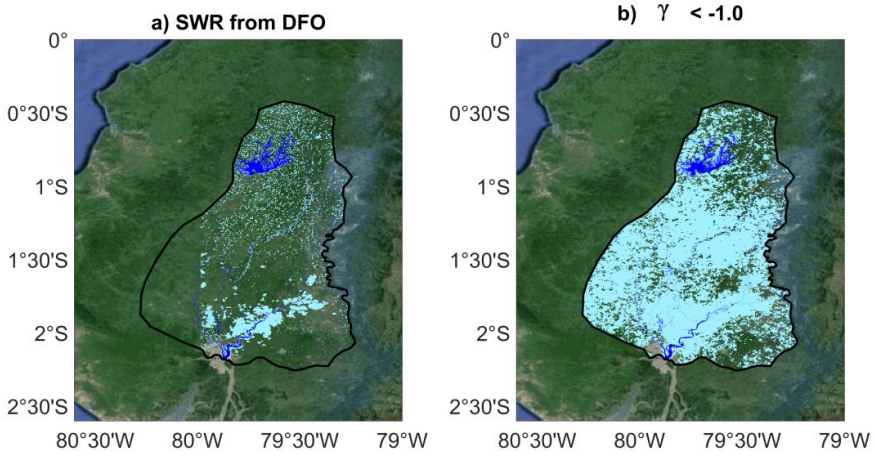

Figure 7. *Cont.*

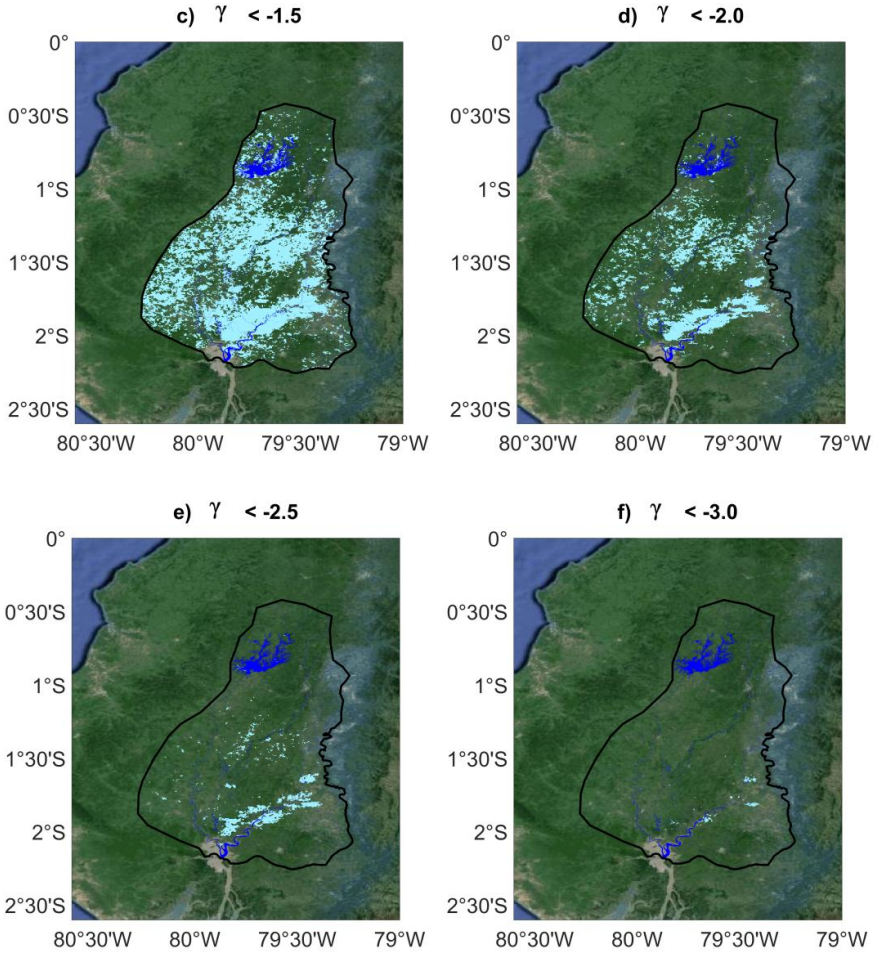

Figure 7. Inundation in the Guayas watershed using the SWR from DFO (**a**). Normalized anomalies of backscattering coefficients (γ) lower than a given threshold appear in light blue. The threshold values equal −1.0 (**b**); −1.5 (**c**); −2.0 (**d**); −2.5 (**e**); and −3.0 (**f**) for 2008. Background image is from Google Maps. Permanent water bodies appear in blue.

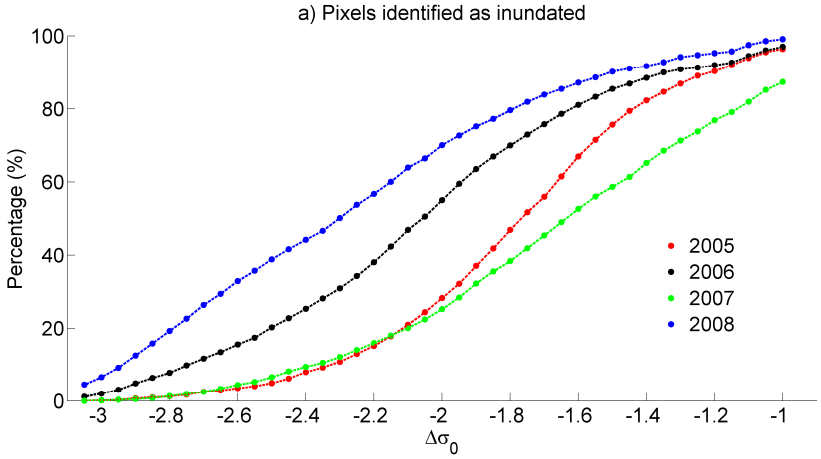

Figure 8. *Cont.*

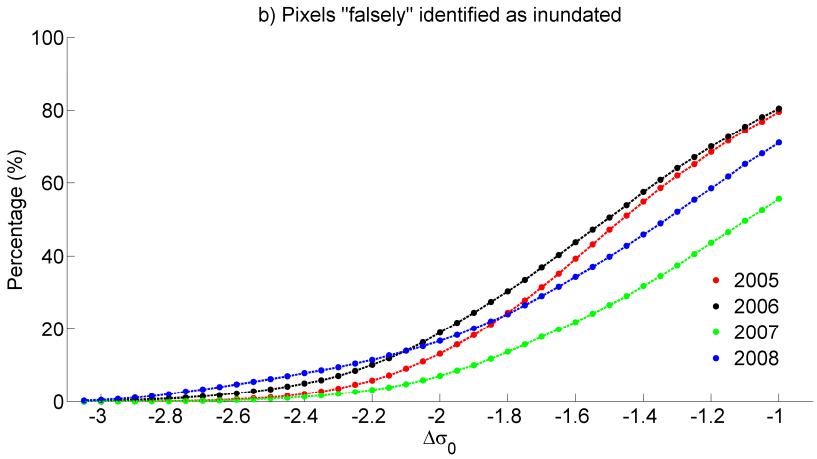

Figure 8. Percentage of pixels detected as inundated (**a**) and falsely identified as inundated during the rainy seasons (December–June) from 2005 to 2008 as a function of the normalized anomaly of backscattering though comparison with the SWR from DFO in the Guayas floodplain (**b**).

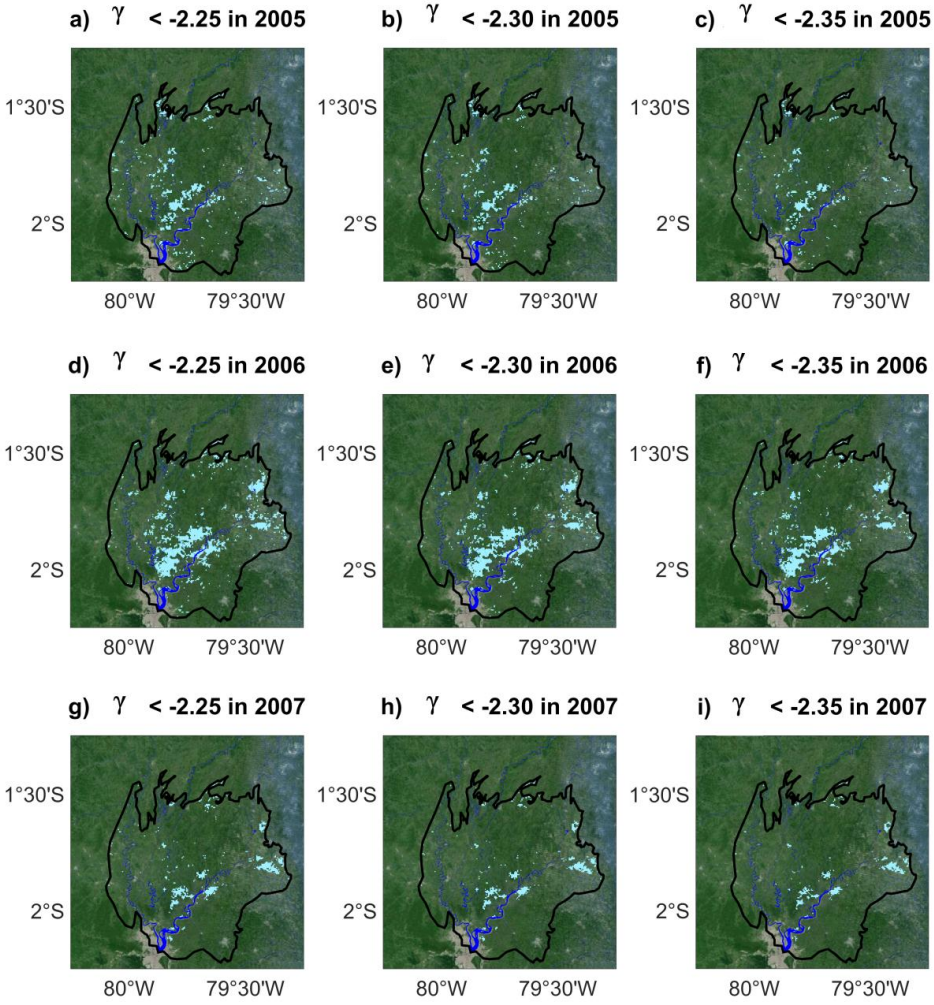

Figure 9. *Cont.*

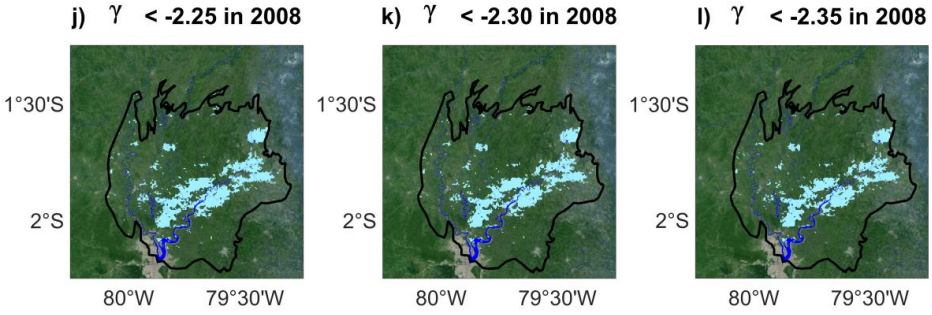

Figure 9. Maps of annual normalized anomalies of backscattering coefficients lower than a given threshold (light blue) in the Guayas floodplain (black line). The threshold values γ equals to -2.25 in 2005 (**a**); 2006 (**d**); 2007 (**g**); and 2008 (**j**); -2.30 in 2005 (**b**); 2006 (**e**); 2007 (**h**); and 2008 (**k**); -2.35 in 2005 (**c**); 2006 (**f**); 2007 (**i**); and 2008 (**l**). Background image is from Google Maps. Permanent water bodies appear in blue.

5.3. Time Variations of Inundated Areas

Using the thresholds determined in Section 5.2, monthly variations of inundation extent were estimated in the Guayas Basin. These monthly variations were obtained as the cumulated extent of the inundated areas observed each month using ASAR images. Time variations of inundated areas during the wet seasons (December–May) from 2005 to 2008 are presented in Figures 10 and 11 for $\gamma = -2.30$. During the observation period, small and disseminated flooded areas were present in December (Figure 10a,g and Figure 11a,g) and January (Figure 10b,h and Figure 11b,h). Largest flood area extents are observed between February and May (Figures 10c–f and 11i–l) with a large interannual variability. Floods generally started in February in the upstream part of the Daule River and the central part of the Quevedo River (Figure 10c,i and Figure 11c,i). Then, floods were mainly located along the central and downstream parts of the Quevedo and Babahoyo Rivers in March and April (Figure 10d,e,j,k and Figure 11d,e,j,k). Floods of smaller extent were detected in May along the Quevedo and Daule Rivers (Figure 10f,l and Figure 11f,l). Inundated areas are most frequently observed along the Babahoyo and Quevedo Rivers and in the Abras de Mantequilla wetland (225 km^2 at 79°45′ W and 1°30′ S). In 2006 and 2008, flooded areas were also detected in the upstream part of the Babahoyo River and along the Daule River (Figures 10g–l and 11g–l). In 2008, very extensive floods were detected in March and April along the Quevedo and Babahoyo river streams.

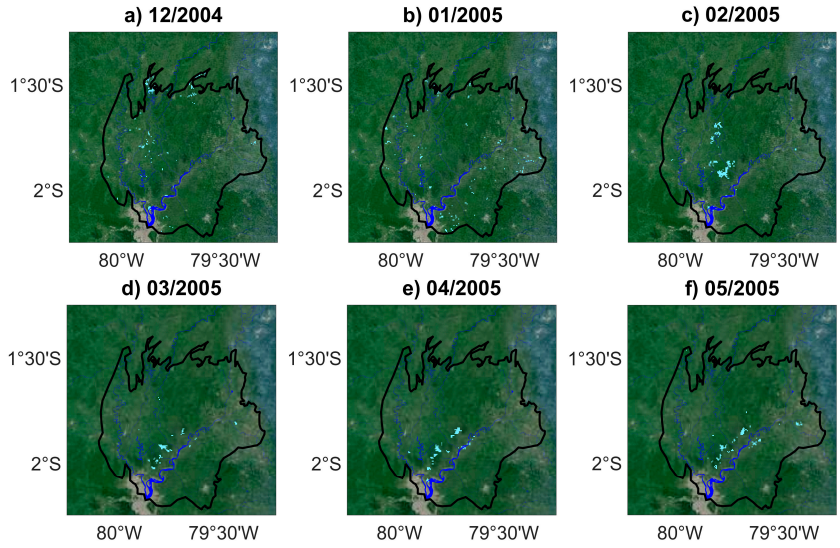

Figure 10. *Cont.*

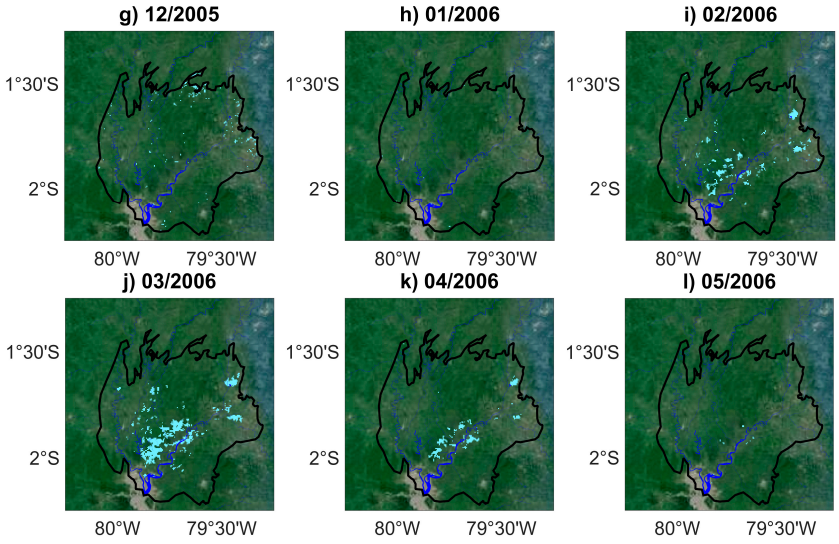

Figure 10. Monthly maps of inundation for normalized anomalies of backscattering coefficients lower than −2.30 (light blue) in the Guayas floodplain (black line) during the wet seasons of 2005 and 2006 (**a**–**f**) from December 2004 to May 2005; and (**g**–**l**) from December 2005 to May 2006. Background image is from Google Maps. Permanent water bodies appear in blue.

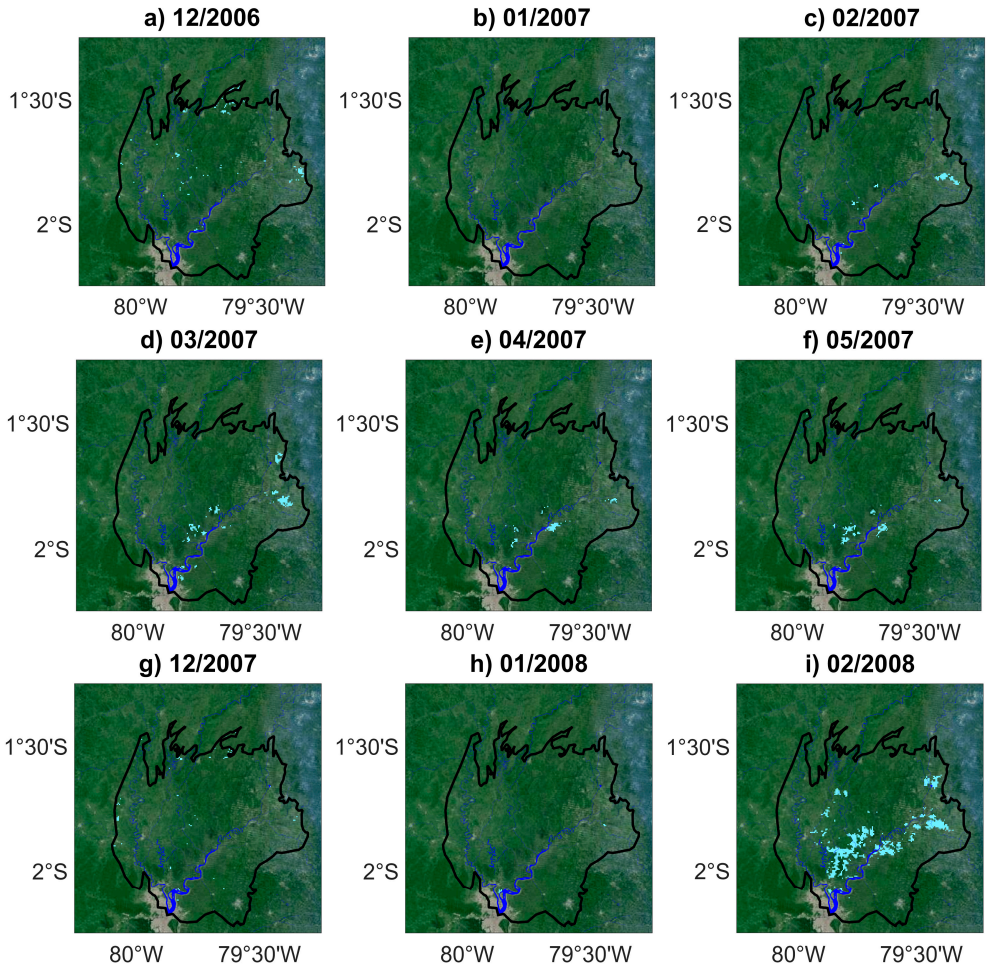

Figure 11. *Cont.*

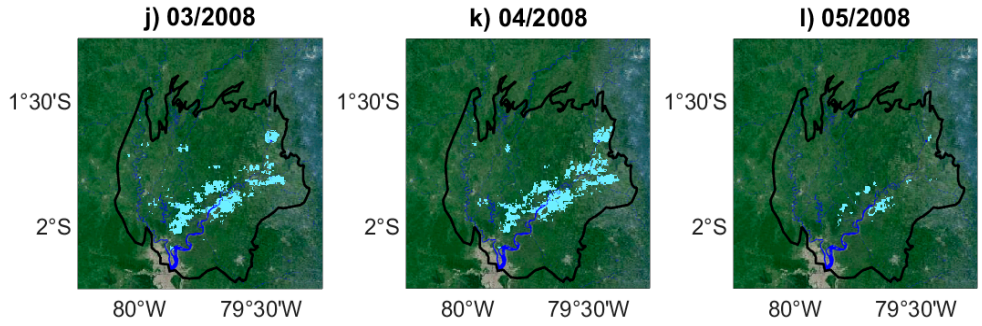

Figure 11. Monthly maps of inundation for normalized anomalies of backscattering coefficients lower than −2.30 (light blue) in the Guayas floodplain (black line) during the wet seasons of 2005 and 2006 (**a**–**f**) from December 2006 to May 2007; and (**g**–**l**) from December 2007 to May 2008. Background image is from Google Maps. Permanent water bodies appear in blue.

RFI maps of the Guayas floodplain were estimated using ENVISAT ASAR GM images acquired during the rainy seasons between December 2004 and June 2008 for the three threshold value used earlier. As they exhibit very similar patterns, only the one obtained using the −2.30 threshold value is presented in Figure 12. Four main areas of large flood occurrence (>25%): the junction between the Babahoyo and Quevedo Rivers, in the upstream north east of Guayaquil, the north and south banks of the Babahoyo River close to the city of Babahoyo, and the upstream eastern part of the floodplain. Secondary maxima (15%) can also be observed along the Daule River.

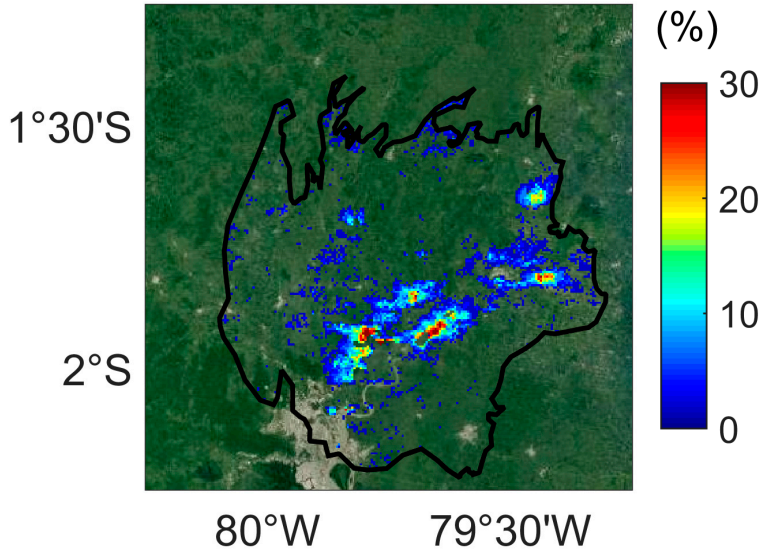

Figure 12. RFI map derived from the ASAR-based inundation extent map for the −2.30 threshold values applied to the normalized anomalies of backscattering coefficients (γ).

Figure 13 shows the time variations of flood extent and rainfall between 2005 and 2008. The hydrological years 2006 and 2008 are characterized by larger flood events (318 and 585 km^2 occurring in March 2006 and April 2008, respectively, as detected using ASAR images) than 2005 and 2007 (53 and 59 km^2 occurring in January 2005 and March 2007, respectively). The total of rainfall for the wet season (December–May) over the whole Guayas Basin for the same time-period were for 757, 1121, 950 and 1366 mm 2005, 2006, 2007 and 2008 respectively. In other terms, these totals of rainfall are 33%, 1% and 16% below the 1963–2009 average rainfall during the rainy season for 2005, 2006 and 2007, respectively, and 20% above it in 2008, meaning that 2005 and 2007 were drier than usual wet seasons, 2006 was a normal wet season and 2008 was a wetter than usual rainy season. When comparing the

inundated areas obtained using the change detection method to the total rainfall during the wet season, a good consistency between these two hydrological variables can be noticed. A correlation of 0.75 was found between these two variables at monthly time-scale, with the total amount of rainfall preceding the flood of one month (inundation extent was set to zero between June and November of each year).

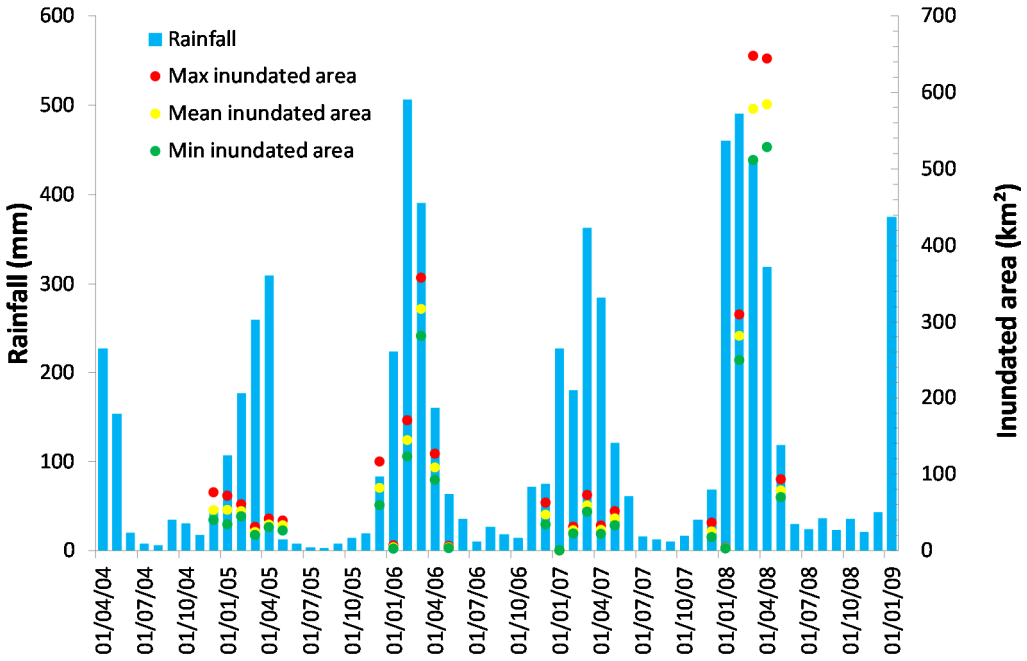

Figure 13. Time series of monthly rainfall (mm—blue bars) and inundation extent (km^2) for three threshold values applied to the normalized anomalies of backscattering coefficients (σ_0) and corresponding to a minimal (−2.35—green dots), a mean (−2.30—yellow dots) and a maximal (−2.25—red dots) inundation area (km^2).

6. Conclusions

ENVISAT ASAR GM images were used to monitor the spatio-temporal dynamics of the flood in the Guayas watershed between 2005 and 2008 applying a change detection method based on the difference in backscattering at C-band between the wet and the dry seasons. First, a supervised classification method was applied to determine the possibility to separate open water from the other classes. Among the different supervised classification techniques applied to determine the land cover in the Guayas Basin using ASAR images acquired during the dry season, the k-nearest neighbors technique provided the better results with an accuracy of 98.2% ± 0.7%. Open water, with a mean backscattering of −11.30 ± 1.68 dB, was clearly separated from the other classes for both the M-statistics and the Jeffries-Matusita distance criteria. This allows the use of the change detection method. In spite of the coarse spatial resolution of these SAR images, inundated areas detection provides consistent results with the sparse information currently available on the distribution of the floodplain in this watershed. Flood most frequently occurred in the eastern part of the floodplain (Andean part), along the Babahoyo river stream, but also on the western part (coastal reliefs) during normal and wetter than usual years. The large interannual variability in the inundation extent, with larger inundated areas detected in 2006 and 2008, was also found to be consistent with the temporal distribution of the rainfall during the wet season.

This study is the first step toward understanding the spatio-temporal (at seasonal and interannual time scales) dynamics of the flood in the Guayas Basin using multi-sensors and multi-resolution SAR images and their relationship with ENSO on a longer time-scale. With the recent launches of Sentinel-1A in April 2014, Sentinel-2A in June 2015 and Sentinel-1B in April 2016, satellite SAR (C-band)

and multispectral images are now globally available at an unprecedented spatio-temporal resolution of a couple of tens of meters every few days. These new datasets will allow better monitoring of land cover and flood locations in watersheds such as the Guayas Basin.

Acknowledgments: This work was supported by SENESCYT under X.R.S. scholarship. The authors thank ESA for providing the ENVISAT ASAR images through the "Monitoring floods in the Guayas basin (Ecuador) using ERS-2 SAR and ENVISAT ASAR images" (ID 13844) proposal.

Author Contributions: Frédéric Frappart and Luc Bourrel conceived, designed the study and processed the ASAR images. Nicolas Brodu and Ximena Riofrío Salazar processed the ASAR images. Frédéric Baup, José Darrozes and Rodrigo Pombosa were involved in the analysis of the results. All authors contributed to the writing of the manuscript.

Conflicts of Interest: The authors declare no conflict of interest.

References

1. Horel, J.D.; Cornejo Garrido, A.G. Convection along the coast of Northern Peru during 1983—Spatial and temporal variation of clouds and rainfall. *Mon. Weather Rev.* **1986**, *114*, 2091–2105. [CrossRef]
2. Bendix, A.; Bendix, J. Heavy rainfall episodes in Ecuador during El Niño events and associated regional atmospheric circulation and SST patterns. *Adv. Geosci.* **2006**, *6*, 43–49. [CrossRef]
3. Bourrel, L.; Rau, P.; Dewitte, B.; Labat, D.; Lavado, W.; Coutaud, A.; Vera, A.; Alvarado, A.; Ordoñez, J. Low-frequency modulation and trend of the relationship between ENSO and precipitation along the Northern to Center Peruvian Pacific coast. *Hydrol. Proc.* **2015**, *29*, 1252–1266. [CrossRef]
4. Rau, P.; Bourrel, L.; Labat, D.; Melo, P.; Dewitte, B.; Frappart, F.; Lavado, W.; Felipe, O. Regionalization of rainfall over the Peruvian Pacific slope and coast. *Int. J. Clim.* **2016**. [CrossRef]
5. Lyon, B.; Barnston, A.G. ENSO and the spatial extent of interannual precipitation extremes in tropical land areas. *J. Clim.* **2005**, *18*, 5095–5109. [CrossRef]
6. Vuille, M.; Raymond, S.B.; Keimig, F. Climate Variability in the Andes of Ecuador and its relation to tropical Pacific and Atlantic Sea Surface Temperature anomalies. *J. Clim.* **2000**, *13*, 2520–2535. [CrossRef]
7. Arteaga, K.; Tutasi, P.; Jiménez, R. Climatic variability related to El Niño in Ecuador—A historical background. *Adv. Geosci.* **2006**, *6*, 237–241. [CrossRef]
8. Carsel, K.M.; Pingel, N.D.; Ford, D.T. Quantifying the benefit of a flood warning system. *Nat. Hazards Rev.* **2004**, *5*, 131–140. [CrossRef]
9. Werner, M.; Reggiani, P.; De Roo, A.; Bates, P.; Sprokkereef, E. Flood forecasting and warning at the river basin and at the European scale. *Nat. Hazards* **2005**, *36*, 25–42. [CrossRef]
10. Rosenqvist, A.; Birkett, C.M. Evaluation of JERS-1 SAR mosaics for hydrological applications in the Congo river basin. *Int. J. Remote Sens.* **2002**, *23*, 1283–1302. [CrossRef]
11. Hess, L.L.; Melack, J.M.; Novo, E.M.L.M.; Barbosa, C.C.F.; Gastil, M. Dual-season mapping of wetland inundation and vegetation for the Central Amazon region. *Remote Sens. Environ.* **2003**, *87*, 404–428. [CrossRef]
12. Frappart, F.; Seyler, F.; Martinez, J.-M.; León, J.G.; Cazenave, A. Floodplain water storage in the Negro River basin estimated from microwave remote sensing of inundation area and water levels. *Remote Sens. Environ.* **2005**, *99*, 387–399. [CrossRef]
13. Betbeder, J.; Gond, V.; Frappart, F.; Baghdadi, N.; Briant, G.; Bartholomé, E. Mapping of Central Africa forested wetlands using remote sensing. *IEEE J. Sel. Top. Appl. Earth Obs. Remote Sens.* **2014**, *7*, 531–542. [CrossRef]
14. Kasischke, E.S.; Smith, K.B.; Bourgeau-Chavez, L.L.; Romanowicz, E.A.; Brunzell, S.; Richardson, C.J. Effects of seasonal hydrologic patterns in south Florida wetlands on radar backscatter measured from ERS-2 SAR imagery. *Remote Sens. Environ.* **2003**, *88*, 423–441. [CrossRef]
15. Bourrel, L.; Phillips, L.; Moreau, S. The dynamics of floods in the Bolivian Amazon Basin. *Hydrol. Proc.* **2009**, *23*, 3161–3167. [CrossRef]
16. Kuenzer, C.; Guo, H.; Huth, J.; Leinenkugel, P.; Li, X.; Dech, S. Flood mapping and flood dynamics of the Mekong delta: ENVISAT-ASAR-WSM based time series analyses. *Remote Sens.* **2013**, *5*, 687–715. [CrossRef]

17. Westerhoff, R.S.; Kleuskens, M.P.H.; Winsemius, H.C.; Huizinga, H.J.; Brakenridge, G.R.; Bishop, C. Automated global water mapping based on wide-swath orbital synthetic-aperture radar. *Hydrol. Earth Syst. Sci.* **2013**, *17*, 651–663. [CrossRef]
18. Schumann, G.; Di Baldassarre, G.; Bates, P.D. The utility of spaceborne radar to render flood inundation maps based on multialgorithm ensembles. *IEEE Trans. Geosci. Remote Sens.* **2009**, *47*, 2801–2807. [CrossRef]
19. Schlaffer, S.; Matgen, P.; Hollaus, M.; Wagner, W. Flood detection from multi-temporal SAR data using harmonic analysis and change detection. *Int. J. Appl. Earth Obs. Geoinf.* **2015**, *38*, 15–24. [CrossRef]
20. Bartsch, A.; Doubkova, M.; Path, C.; Sabel, D.; Wagner, W.; Wolski, P. River flow and wetland monitoring with ENVISAT ASAR global mode in the Okavango Basin and Delta. In Proceedings of the Second IASTED Africa WRM Conference, Gaborone, Botswana, 8–10 September 2008; Acta Press: Anaheim, CA, USA, 2008; Volume 602, pp. 152–156.
21. Bartsch, A.; Wagner, W.; Scipal, K.; Pathe, C.; Sabel, D.; Wolski, P. Global monitoring of wetlands—The value of ENVISAT ASAR Global mode. *J. Environ. Manag.* **2009**, *90*, 2226–2233. [CrossRef] [PubMed]
22. O'Grady, D.; Leblanc, M.; Gillieson, D. Use of ENVISAT ASAR Global Monitoring Mode to complement optical data in the mapping of rapid broad-scale flooding in Pakistan. *Hydrol. Earth Syst. Sci.* **2011**, *15*, 3475–3494. [CrossRef]
23. Rossel, F.; Cassier, E.; Gómez, G. Las inundaciones en la zona costera ecuatoriana: Causas—Obras de protección existentes y previstas. *Bulletin de l'Institut Français d'Études Andines* **1996**, *25*, 399–420.
24. Borbor-Cordova, M.; Boyer, E.; McDowell, W.; Hall, C. Nitrogen and phosphorus budgets for a tropical watershed impacted by agricultural land use: Guayas, Ecuador. *Biogeochemistry* **2006**, *79*, 135–161. [CrossRef]
25. Bourrel, L.; Melo, P.; Vera, A.; Pombosa, R.; Guyot, J.-L. Study of the erosion risks of the Ecuadorian Pacific coast under the influence of ENSO phenomenom: Case of the Esmeraldas and Guayas basins. In Proceedings of the International Conference on the Status and Future of the World's Large Rivers, Vienna, Austria, 11–14 April 2011.
26. Waite, P.J. Competition for water resources of the Rio Guayas, Ecuador. In *Optimal Allocation of Water Resources, Proceedings of the Exeter Symposium, Exeter, UK, 19–30 July 1982*; Lowing, M.J., Ed.; IAHS Publications No. 135; IAHS Redbooks: Exeter, UK, 1982; pp. 79–88.
27. Twilley, R.R.; Cárdenas, W.; Rivera-Monroy, V.H.; Espinoza, J.; Suescum, R.; Armijos, M.M.; Solórzano, L. The Gulf of Guayaquil and the Guayas river estuary, Ecuador. In *Coastal Marine Ecosystems of Latin America. Ecological Studies*; Seeliger, U., Kjerfve, B., Eds.; Springer: Berlin, Germany, 2001; pp. 245–263.
28. Desnos, Y.-L.; Buck, C.; Guijarro, J.; Suchail, J.-L.; Torres, R.; Attema, E. ASAR—Envisat's Advanced Synthetic Aperture Radar. Building on ERS achievements towards future watch missions. *ESA Bull.* **2000**, *102*, 91–100.
29. Pathe, C.; Wagner, W.; Sabel, D.; Doubkova, M.; Basara, J.B. Using ENVISAT ASAR Global Mode Data for Surface Soil Moisture Retrieval Over Oklahoma, USA. *IEEE Trans. Geosci. Remote Sens.* **2009**, *47*, 468–480. [CrossRef]
30. Baup, F.; Mougin, E.; de Rosnay, P.; Hiernaux, P.; Frappart, F.; Frison, P.-L.; Zribi, M.; Viarre, J. Mapping surface soil moisture over the Gourma mesoscale site (Mali) by using ENVISAT ASAR data. *Hydrol. Earth Syst. Sci.* **2011**, *15*, 603–616. [CrossRef]
31. Henry, J.B.; Chastanet, P.; Fellah, K.; Desnos, Y.-L. Envisat multi-polarized ASAR data for flood mapping. *Int. J. Remote Sens.* **2006**, *27*, 1921–1929. [CrossRef]
32. EOLI (Earth Observation Link). The European Space Agency's Client for Earth Observation Catalogue and Ordering Services. Available online: https://earth.esa.int/web/guest/eoli (accessed on 1 April 2013).
33. Tapia Aldas, J.C. Modelización Hidrológica de un Area Experimental en la Cuenca del Rio Guayas en la Producción de Caudales y Sedimentos. Ph.D. Thesis, Universidad Nacional de la Plata, La Plata, Argentina, 2012.
34. Brakenridge, G.R. *Global Active Archive of Large Flood Events, Dartmouth Flood Observatory*; University of Colorado: Boulder, CO, USA, 2012.
35. Brakenridge, G.R.; Anderson, E. MODIS-based flood detection, mapping, and measurement: The potential for operational hydrological applications. In *Transboundary Floods: Reducing the Risks through Flood Management*; Marsalek, J., Stancalie, G., Balint, G., Eds.; Springer: Dordrecht, The Netherlands, 2006; p. 16.
36. *Flood Observatory Database*; University of Colorado: Boulder, CO, USA, 2015. Available online: http://floodobservatory.colorado.edu (accessed on 21 September 2015).

37. Rosich, B.; Meadows, P. *Absolute Calibration of ASAR Level 1 Products*; ESA/ESRIN, ENVI-CLVL-EOPG-TN-03-0010; European Space Agency: Noordwijk, The Netherland, 2004. Available online: https://earth.esa.int/web/guest/-/absolute-calibration-of-asar-level-1-products-generated-with-pf-asar-4503 (accessed on 21 March 2013).
38. European Space Agency (ESA). *Absolute Calibration of ASAR Level 1 Products Generated with PF-ASAR*, 15th ed.; European Space Agency: Rome, Italy, 2004.
39. Baghdadi, N.; Bernier, M.; Gauthier, R.; Neeson, I. Evaluation of C-band SAR data for wetlands mapping. *Int. J. Remote Sens.* **2001**, *22*, 71–88. [CrossRef]
40. Ulaby, F.T.; Moore, R.K.; Fung, A.K. *Microwave Remote Sensing, Active and Passive, 2, Radar Remote Sensing and Surface Scattering and Emission Theory*; Addison-Wesley: Reading, MA, USA, 1982.
41. Shi, J.; Dozier, J.; Rott, H. Snow mapping in Alpine regions with Synthetic Aperture Radar. *IEEE Trans. Geosci. Remote Sens.* **1994**, *32*, 152–158.
42. Lee, J.S. Digital image smoothing and the sigma filter. *Comput. Vis. Graph. Image Process.* **1983**, *24*, 255–269. [CrossRef]
43. Frappart, F.; Bourrel, L.; Riofrio Salazar, X.; Baup, F.; Darrozes, J.; Pombosa, R. Spatiotemporal dynamics of the floods in the Guayas watershed (Ecuadorian Pacific Coast) using ASAR images. In Proceedings of the 2015 IEEE International Geoscience and Remote Sensing Symposium (IGARSS), Milan, Italy, 26–31 July 2015; pp. 2515–2518.
44. Kaufman, Y.J.; Remer, L.A. Detection of forests using mid-IR reflectance: An application for aerosol studies. *IEEE Trans. Geosci. Remote Sens.* **1994**, *32*, 672–683. [CrossRef]
45. Miettinen, J.; Liew, S.C. Separability of insular South-east Asian woody plantation species in the 50 m resolution ALOS PALSAR mosaic product. *Remote Sens. Lett.* **2011**, *2*, 299–307. [CrossRef]
46. Richards, J.A. *Remote Sensing Digital Image Analysis*; Springer: Berlin, Germany, 1999.
47. Gianinetto, M.; Villa, P.; Lechi, G. Postflood damage evaluation using Landsat TM and ETM+ data integrated with DEM. *IEEE Trans. Geosci. Remote Sens.* **2006**, *44*, 236–243. [CrossRef]
48. Papa, F.; Frappart, F.; Malbéteau, Y.; Shamsudduha, M.; Venugopal, V.; Sekhar, M.; Ramillien, G.; Prigent, C.; Aires, F.; Pandey, R.K.; et al. Satellite-derived Surface and Sub-surface Water Storage in the Ganges-Brahmaputra River Basin. *J. Hydrol. Reg. Stud.* **2015**, *4*, 15–35. [CrossRef]
49. Skakun, S.; Kussul, N.; Shelestov, A.; Kussul, O. Flood hazard and flood risk assessment using a time series of satellite images: A case study in Namibia. *Risk Anal.* **2014**, *34*, 1521–1537. [CrossRef] [PubMed]
50. Arias-Hidalgo, M.; Gonzalo, V.-C.; van Griensven, A.; Solórzano, G.; Villa-Cox, R.; Mynett, A.E.; Debels, P. A decision framework for wetland management in a river basin context: The "Abras de Mantequilla" case study in the Guayas River Basin, Ecuador. *Environ. Sci. Policy* **2013**, *34*, 103–114. [CrossRef]